Title
Performance evaluation of dual-ended readout PET detectors based on BGO arrays with different reflector arrangements

Journal
Physics in Medicine and Biology, 66(21)

ISSN
0031-9155

Authors
Du, Junwei
Wang, Qian
Liu, Chih-Chieh
et al.

Publication Date
2021-11-07

DOI
10.1088/1361-6560/ac2c9c

Peer reviewed

HHS Public Access
Author manuscript
Phys Med Biol. Author manuscript; available in PMC 2022 October 19.

Published in final edited form as:
Phys Med Biol. ; 66(21): . doi:10.1088/1361-6560/ac2c9c.

Performance evaluation of dual-ended readout PET detectors based on BGO arrays with different reflector arrangements

Junwei Du, **Qian Wang**, **Chih-Chieh Liu**, **Jinyi Qi**, **Simon R. Cherry**
Department of Biomedical Engineering, University of California at Davis, Davis, CA 95616, USA

Abstract

Dual-ended readout depth-encoding detectors based on bismuth germanate (BGO) scintillation crystal arrays are good candidates for high-sensitivity small animal positron emission tomography (PET) used for very-low-dose imaging. In this paper, the performance of three dual-ended readout detectors based on 15 × 15 BGO arrays with three different reflector arrangements and 8 × 8 silicon photomultiplier (SiPM) arrays were evaluated and compared. The three BGO arrays, denoted wo-ILG (without internal light guide), wp-ILG (with partial internal light guide), and wf-ILG (with full internal light guide), share a pitch size of 1.6 mm and thickness of 20 mm. Toray E60 with a thickness of 50 μm was used as inter-crystal reflector. All reflector lengths in the wo-ILG and wf-ILG BGO arrays were 20 and 18 mm, respectively; the reflectors in the wp-ILG BGO array were 18 mm at the central region of the array and 20 mm at the edge. By using 18mm reflectors, part of the crystals in the wp-ILG and wf-ILG BGO arrays worked as internal light guides. The results showed that the detector based on the wo-ILG BGO array provided the best flood histogram. The energy, timing and DOI resolutions of the three detectors were similar. The energy resolutions (FWHM value) based on the wo-ILG, wp-ILG and wf-ILG BGO arrays were 27.2 ± 3.9 %, 28.7 ± 4.6 %, and 29.5 ± 4.7 %, respectively. The timing resolutions (FWHM value) were 4.7 ± 0.5 ns, 4.9 ± 0.5 ns, and 5.0 ± 0.6 ns, respectively. The DOI resolution (FWHM value) were 3.0 ± 0.2 mm, 2.9 ± 0.2 mm, and 3.0 ± 0.2 mm, respectively. Over all, the wo-ILG detector provided the best performance.

Keywords

PET; DOI; BGO; LYSO

1. Introduction

Bismuth germanate (BGO) based detectors are promising candidates for building high-sensitivity small animal positron emission tomography (PET) scanners used for very-low-dose imaging (Gambhir *et al* 1999, Jung *et al* 2020, van Dongen *et al* 2020). Commonly used lutetium oxyorthosilicate (LSO) and lutetium yttrium oxyorthosilicate (LYSO) scintillation crystals are not best-suited for very-low-dose PET imaging, due to their intrinsic radiation caused by ^{176}Lu (Bao and Chatziioannou 2010, Freedenberg *et al* 2014). Compared to LSO and LYSO, BGO has much lower intrinsic radiation (de Marcillac *et al*

jwdu@ucdavis.edu .

2003), higher stopping power, and lower cost (Lewellen 2008, Du *et al* 2009, Cherry *et al* 2012), which make BGO a better choice for high-sensitivity small animal PET scanners for very-low-dose imaging, for applications such as cell tracking (Jung *et al* 2020, van Dongen *et al* 2020), and gene expression imaging (Gambhir *et al* 1999, Blasberg 2002, Sharma *et al* 2002).

To obtain uniform and high spatial resolution across the field-of-view (FOV) of preclinical PET scanners, as well as high-sensitivity, detectors with thick crystals and depth-of-interaction (DOI) information are required. Dual-ended readout detectors are good candidates for building PET scanners that provide uniform and high spatial resolution across the FOV (Shao *et al* 2014, Ouyang *et al* 2016, Du *et al* 2018b, Kuang *et al* 2020). However, the low light yield of BGO makes designing high-resolution BGO based dual-ended readout PET detectors difficult, as the depth-encoding in these detectors requires a partial loss in light collection efficiency along the length of the crystals.

Compared to dual-ended readout detectors based on LSO or LYSO arrays that have been well studied (Ren *et al* 2014, Kuang *et al* 2019, Du *et al* 2019, Li *et al* 2020, Kang *et al* 2020), dual-ended readout detectors based on BGO arrays have received relatively less attention. In a previous study, interestingly, dual-ended BGO and LYSO detectors showed different behavior: LYSO arrays with polished lateral surfaces and Toray reflector provided ~ 2 mm DOI resolution, however, BGO arrays with polished lateral surfaces and Toray reflector could not provide DOI resolution (Du *et al* 2020). In that work, we developed the first batch of dual-ended readout detectors using BGO arrays with 2.2 mm pitch coupled to silicon photomultiplier (SiPM) arrays with the same pitch using the 1:1 coupling method, and these detectors showed promising performance (Du *et al* 2020). The drawback of the 1:1 coupling method is the spatial resolution of the PET detector is limited by the pitch size of SiPM arrays. To improve the spatial resolution and use as few electronic channel as possible, the light-sharing method is widely used to resolve crystal arrays with a pitch size smaller than the pitch size of photodetector arrays (Du *et al* 2018a, Pizzichemi *et al* 2019, LaBella *et al* 2020, Yoshida *et al* 2020). In light-sharing detectors, light guides are required to spread the scintillation photons to multiple SiPM pixels. Internal and external light guides have both been employed in the light-sharing method (Wong *et al* 2015, Du *et al* 2019). Compared to the external light guide that is typically a transparent layer between the scintillation crystal array and SiPM, the internal light guide method exploits the transparency of crystals themselves to allow the light sharing among crystals by leaving the crystal ends unwrapped by reflectors and can improve the performance of the detector by reducing the interfaces between the crystal arrays and the SiPM arrays. Different reflector arrangements in the crystal array can potentially yield different light distributions and therefore detector performance.

In this paper, the performance of three dual-ended readout detectors based on BGO arrays with different reflector arrangements were evaluated and compared in terms of the flood histogram quality, energy, timing and DOI resolutions. Two of the three BGO arrays were fabricated with different internal light guides, and the third one was fabricated without internal light guides. All BGO arrays had a pitch size of 1.6 mm and SiPM arrays with a pitch size of 3.2 mm as the photodetectors.

2. Materials and Methods

2.1. Dual-ended readout detectors

Figure 1 shows photographs and figure 2 shows the schemas of the reflector arrangements of the three 15 × 15 BGO arrays of 1.54 × 1.54 × 20 mm^3 BGO crystals. The BGO material was grown by Shanghai SICCAS High Technology Corporation, China, and the BGO arrays were fabricated by Sichuan Tianle Photonics Co., Ltd, China. All the BGO arrays had a pitch size of 1.6 mm. The four lateral sides of the BGO crystals were unpolished, and the two end surfaces were polished. Toray E60 (Toray Industries, Inc., Japan) with a thickness of 50 μm was used as the inter-crystal reflector, and 5 μm thick optical glue OP-30 (Dymax Corporation, USA) was used to glue the reflectors onto the crystals.

The three BGO arrays shown in figures 1 and 2 (from left to right) were denoted as wo-ILG, wp-ILG, and wf-ILG BGO arrays, respectively, where “wo”, “wp” and “wf” stand for “without”, “with partial” and “with full”, respectively, and ILG is the abbreviation for internal light guide. The dual-ended readout detectors based on these BGO arrays were named correspondingly. The thickness of the internal light guide was chose to be 1 mm based on our previous experiment results (Du *et al* 2019).

The wo-ILG BGO array was chose as a reference detector, which is the easiest array to be fabricated. The wf-ILG BGO array was used to mimic the wo-ILG BGO array coupled to an external light guide. The wp-ILG BGO array was designed to improve the resolve ability for the outmost rows/columns crystals, which was used to mimic external light guide with special cuts.

Two Hamamatsu S14161-0305-08-HS SiPM arrays were used to measure the light output of the BGO arrays. Each Hamamatsu S14161-0305-08-HS SiPM array has 8 × 8 SiPMs with a pitch size of 3.2 mm, and each SiPM has an active area of 3 × 3 mm^2. The microcell size of the SiPMs is 50 um and the breakdown voltage is 27.5 V at 21°C. Each BGO array was coupled to the center of the SiPM arrays using optical grease BC-631 (Saint-Gobain S.A., USA) with a reflective index of 1.465. 3D printed holders were used to keep the relative position of the BGO array and the SiPM arrays fixed for different measurements.

Figure 3 shows the relative position of the SiPM arrays and the BGO array. As the pitch size of the BGO arrays is half the pitch size of the SiPM arrays, 64 of the BGO elements were coupled to the center of SiPMs, 112 BGO elements were coupled across two adjacent SiPMs, and 49 BGO elements were coupled at the intersection of four SiPMs.

2.2. Readout electronics

Figure 4 shows the schema of the readout electronics. To simplify the readout electronics, the 128 SiPM signals from each dual-ended readout detector were reduced to 8 position signals and 1 timing signal using a signal multiplexing readout method (Popov *et al* 2003, Du *et al* 2016, 2019). For each dual-ended readout detector, the timing signal is the sum of all the SiPM signals. The timing information of the dual-ended readout detector and the PMT based reference detector were both picked off using constant fractional discriminators (CFDs) (model 584, ORTEC, USA), and used as the start and stop signals for the time-to-amplitude-convector (TAC) (model 566, ORTEC), respectively. The 8 position signals of the dual-ended readout detector, the energy signal of the reference detector, and the TAC output were digitized by a 32-channel digitizer DT5740D (CAEN S.p.A., Italy) at a speed of 62.5 megasamples per second (MSPS).

2.3 Experimental methods

During all experiments, the dual-ended detector under evaluation, and the front-end readout board were located in a light-tight enclosure. The temperate inside the enclosure was controlled at 23.6 ± 0.2 °C by blowing cool-dry air into the enclosure and monitored using a thermocouple.

A 13 μCi ^{22}Na source with an active diameter of 0.25 mm was used for all experiments. All experiments were done at a bias voltage of 41.0 V, which was selected based on our previous studies to obtain the best flood histogram (Du *et al* 2019). A 20 ns timing window and a 350–750 keV energy window were used to select events.

2.3.1 Flood histogram—The flood histogram and timing resolution data were acquired simultaneously using a reference detector consisting of a Hamamatsu PMT R13449-10 coupled to an LYSO cylinder with a diameter of 20 mm and a length of 5 mm. The LYSO cylinder was wrapped with 6 layers of Teflon to maximize the light output. For each measurement, 1.2 M events were collected for further processing.

The gamma photon interaction positions (x, y) were calculated using the following formula:

$$x = \frac{x_{front}E_{front}^{n} + x_{rear}E_{rear}^{n}}{E_{front}^{n} + E_{rear}^{n}}, y = \frac{y_{front}E_{front}^{n} + y_{rear}E_{rear}^{n}}{E_{front}^{n} + E_{rear}^{n}} \quad (1)$$

$$x_{front} = \frac{X_{front}^{+} - X_{front}^{-}}{X_{front}^{+} + X_{front}^{-}}, y_{front} = \frac{Y_{front}^{+} - Y_{front}^{-}}{Y_{front}^{+} + Y_{front}^{-}} \quad (2)$$

$$x_{rear} = \frac{X_{rear}^{+} - X_{rear}^{-}}{X_{rear}^{+} + X_{rear}^{-}}, y_{rear} = \frac{Y_{rear}^{+} - Y_{rear}^{-}}{Y_{rear}^{+} + Y_{rear}^{-}} \quad (3)$$

$$E_{front} = X_{front}^{+} + X_{front}^{-} + Y_{front}^{+} + Y_{front}^{-} \quad (4)$$

$$E_{rear} = X_{rear}^{+} + X_{rear}^{-} + Y_{rear}^{+} + Y_{rear}^{-} \quad (5)$$

where X_{front}^{+}, X_{front}^{-}, Y_{front}^{+}, and Y_{front}^{-} were the four position signals of the SiPM array coupled to the front end of the BGO array, and X_{rear}^{+}, X_{rear}^{-}, Y_{rear}^{+} and Y_{rear}^{-} were the four position signals of the SiPM array coupled to the rear end of the BGO array (Popov *et al* 2003, Du *et al* 2019). E_{front} and E_{rear} were the total energies detected by the two SiPM arrays coupled to the front and rear end of the BGO array, respectively. E_{front}^{n} and E_{rear}^{n} (n = 0, 1, 2, …, 10) were the weighting factors for the interaction positions calculated using the the two SiPM arrays coupled to the front and rear ends of the BGO array, respectively.

To compare the flood histograms, flood histogram qualities were calculated using the ratios of the distances to widths of the crystal spots in the flood histograms (Du *et al* 2016).

2.3.2 Energy resolution—The energy (E) of the gamma photon deposited in the BGO array was calculated using

$$E = E_{front} + E_{rear} \tag{6}$$

Energy resolution was calculated for each crystal after the events were binned into each crystal using a look-up table. The energy resolution was calculated as the ratio of the full width at half maximum (FWHM) to the centroid value of the energy spectrum, both of which were extracted from a Gaussian fit to the 511 keV photopeak of the energy spectra. The average and standard deviation values of the energy resolutions across all crystal elements in the BGO array were used as a measure of the energy resolution of the detector.

2.3.3 Timing resolution—The timing resolution, in coincidence with the PMT based reference detector, was also calculated for each crystal. The timing resolution was measured as the FWHM of the timing spectrum, which was extracted from a Gaussian fit to the timing spectrum. The average and standard deviation values of the timing resolutions across all crystals were used to measure the timing resolution of the detector. The timing resolution of two identical reference detectors was 200 ± 10 ps.

2.3.4 DOI resolution—The DOI resolution was measured using a reference detector consisting of a Hamamatsu R13449-10 PMT and a 0.5 × 20 × 20 mm^3 polished LYSO wrapped with 6 layers of Teflon (figure 4) (Yang *et al* 2019). A ^{22}Na point source was placed between the BGO and the reference detectors with a distance of 100 mm from both of the detectors (Du *et al* 2018a). The DOI data was obtained at 9 depths, from 2 mm to 18 mm, and in 2 mm intervals. At each depth, 1×10^6 events were acquired.

As the BGO arrays were irradiated from one side and gamma photons are attenuated as they pass through the BGO array, only a fraction of BGO elements detected adequate events for analysis as shown in figure 5. The 60 crystals in the white rectangle were used as representative crystals to measure the DOI resolution of the BGO array.

The DOI resolution was calculated using

$$DOI = a\frac{E_{front} - E_{rear}}{E_{front} + E_{rear}} + b \tag{7}$$

where, a and b were fitting parameters used to model the DOI and the ratio of the two energies E_{front} and E_{rear} (Shao *et al* 2008, Du *et al* 2020). To calculate the DOI resolution, events were assigned to each crystal using a look-up table, and *a* and *b* were obtained for each crystal and were different for different crystal elements.

The DOI resolution was calculated using the FWHM of the Gaussian fit to the DOI distribution profile of a crystal at one depth. The average and standard deviation values of DOI resolutions across all depths for a given crystal were used to measure the DOI resolution of this crystal, and the average and standard deviation values of DOI resolutions across all depths and all crystals of a BGO array were used as a measure of the DOI resolution of the BGO detector.

3. Results

2.3.1 Flood histogram

Figure 6 shows the flood histograms of the three detectors obtained using E_{front}^2 and E_{rear}^2 as the weighting factors for the interaction positions calculated using the signals from the two SiPM arrays coupled to the front and rear ends of the BGO array (equation 1). All the BGO elements in the three BGO arrays were clearly resolved, and the wo-ILG detector had the best flood histogram. The flood histogram quality values of the three flood histograms shown in figure 6 were 2.1 ± 0.3, 1.8 ± 0.2, and 1.6 ± 0.2, respectively.

The position profiles of crystals in the 6th column are shown in figure 7. It is clear that the wo-ILG detector had the best crystal resolvability, especially for the edge crystals. The peak-to-valley ratios of the position profiles of the wo-ILG, wp-ILG and wf-ILG detectors were 4.6 ± 1.1, 4.0 ± 1.4, and 3.1 ± 0.6, respectively.

Figure 8 shows the flood histogram quality values of the three detectors obtained using different weighting factors for the interaction positions calculated using the two SiPM arrays (equation 1). The flood histogram quality values first increases quickly and then decreases slowly with increasing power of n, and the highest flood histogram quality values were obtained using a power of 2, due to the light distribution changes approximately with square of distance.

2.3.2 Energy resolution

Figure 9 shows the energy resolution and the 511 keV photopeak position for each crystal of the three detectors. The energy resolution and the 511 keV photopeak position were both crystal dependent, which was caused by the difference of the light collection and the non-uniformity of the BGO arrays. The average energy resolutions of the wo-ILG, wp-ILG, and wf-ILG detectors were 44.3 ± 6.6 %, 44.9 ± 6.4 %, and 43.9 ± 6.4 %, respectively.

Figure 10 shows the average energy resolutions (top row) and the 511 keV photopeak position (botton row) across all crystal elements obtained at different depths. The average energy resolution and the 511 keV photopeak position are both depth-dependent. With the DOI correction, the average energy resolutions of the wo-ILG, wp-ILG and wf-ILG detectors were 27.2 ± 3.9 %, 28.7 ± 4.6 %, and 29.5 ± 4.7 %, respectively. The DOI correction greatly improved the energy resolution.

2.3.3 Timing resolution

Figure 11 shows the timing resolution for each crystal of the three detectors, and figure 12 shows the average timing resolution obtained at different depths. The timing resolutions were crystal and depth dependent, which corresponds to the signal amplitude of 511 keV photons shown in figures 9 (bottom row) and 10 (right). The larger the signals, the better the timing resolution. The average timing resolutions without DOI corrections of the wo-ILG, wp-ILG and wf-ILG detectors were 4.8 ± 0.4 ns, 5.0 ± 0.4 ns, and 5.1 ± 0.5 ns, respectively, and these improved marginally with DOI correction to 4.7 ± 0.5 ns, 4.9 ± 0.5 ns, and 5.0 ± 0.6 ns, respectively.

2.3.4 DOI resolution—Figure 13 shows the average DOI resolutions across the 9 depths of the 60 selected crystals. As the BGO arrays were irradiated from one side, the BGO elements closer to the source had better DOI resolutions (left part in figure 13), as the detection of scattered photons and the divergence of the collimating beam both increase with increasing penetration into the crystal arrays (Yang *et al* 2019, Du *et al* 2018a). The average DOI resolution across all depths and all crystals of the wo-ILG, wp-ILG and wf-ILG detectors were 3.0 ± 0.2 mm, 2.9 ± 0.2 mm, and 3.0 ± 0.2 mm, respectively.

4. Discussion

The performance in terms of flood histogram quality, energy, timing and DOI resolution of the three detectors based on BGO arrays with different reflector arrangements are summarized in Table I. Overall, the wo-ILG detector had the best flood histogram, and the energy, timing and DOI resolutions of the three detectors were similar.

The flood histograms showed that all the crystal elements in the BGO arrays were clearly resolved (figure 6). The wo-ILG detector had the best flood histogram, as the reflector length was the same as the BGO thickness, which limited the spread of scintillation photons. The average of the two interaction positions calculated using the two SiPM arrays coupled to both ends of the scintillator arrays has been widely used to determine the interaction positions of the gamma photon (Shao *et al* 2014, Kyme *et al* 2017, Du *et al* 2018a, Yang *et al* 2019, Li *et al* 2020), however, in this study, our results showed that better flood histograms can be obtained by weighting the interaction positions using the energies (figure 8 and equation 1).

The energy resolutions of the three detectors without the DOI correction were ~ 44 %. They were improved to 27 – 30 % with the DOI correction. The energy resolution in this study is worse than the energy resolutions of other BGO detectors with similar pitch (Zhang *et al* 2002, Zhang *et al* 2010, Gu *et al* 2013, González *et al* 2016), mainly due to the fact that the BGO elements used here that have unpolished lateral surfaces and Toray reflectors which provide good DOI resolution, however, reduce the number of scintillation photons reaching the SiPMs and shift the 511 keV photopeak as a function of depth (figure 10 (right)).

The light outputs of wp-ILG and wf-ILG were almost identical as the reflector arrangement are similar, except for the outmost rows/columns (figure 2). Without using the internal light guide, most scintillation photons are restricted to one crystal, the light loss is less. While using the internal light guide, scintillation photons can spread to more crystals in the internal light guide part and be absorbed by the 60 um thick optical glue between the crystals before reaching the SiPMs (the optical glue used by the manufacturer of the detectors showing some light yellow color after UV light irradiation). Hence, the light loss can be higher.

The timing resolution with and without the DOI correction had similar values of ~ 5 ns, which means the DOI correction for timing resolution will not be necessary when the detectors are used to build PET scanners. The timing resolution is not comparable to the start-of-the-art PET detector based on LYSO or LSO crystals (Pizzichemi *et al* 2019, Gundacker *et al* 2016), due mainly to the lower light yield and slower decay time of the BGO crystal. PET detectors based on BGO crystals that use Cherenkov photons as a timing trigger can provide a good timing resolution (Kwon *et al* 2016, Brunner and Schaart 2017); however, these detectors require high-bandwidth and ultra-low noise readout electronics, which makes it difficult to design multi-channel electronics. We used a signal multiplexing readout to simplify the readout electronics, which also contributed to the worse timing resolution. If the SiPM signals were read out individually and the timing was picked off from each SiPM signal using application-specific integrated circuits (ASICs), the timing resolution could be improved. However, there are currently no ASICs designed for dual-ended available.

The DOI resolutions were all ~ 3 mm, which is a typical value for dual-ended detectors based on 20-mm-thick LYSO or BGO crystals (Li *et al* 2020, Kang *et al* 2020, Du *et al* 2020).

In our studies, the wp-ILG detector and the wf-ILG detector with the internal light guide were designed to improve the uniformity of the 511 keV photopeak positions, as 24.3% of the cross-sectional area of those BGO elements coupled across four SiPMs were coupled to the deadspace of the SiPM arrays. However, the 511 keV photopeak positions of the wo-ILG detector did not show patterns related to the deadspace of the SiPMs (figure 9), which can be explained by the non-uniformity of the BGO array and also the 0.15 mm silicon resin windows of the SiPM arrays that worked as light guides to spread the scintillation photons.

5. Conclusion

In this study, the performance of three dual-ended readout detectors based on BGO arrays with different reflector arrangements were compared. The results showed that the energy, timing and DOI resolutions of the three detectors were similar. However, compared to the wp-ILG and the wf-ILG detectors with internal light guides, the wo-ILG detector, which had no internal light guide, provided a better flood histogram. In addition, the wo-ILG BGO arrays are easier to fabricate and less expensive, hence, we will use the wo-ILG detectors as the basis to build a total-body small-animal PET scanner for low-dose imaging.

Although the way to implement the internal light was used for dual-ended readout BGO detector in this paper, it can also be used for other PET detectors, either dual-ended readout or single-ended readout, that require external light guides.

Acknowledgements

This work was funded by NIH grant R01 EB028806.

References

Bao Q and Chatziioannou AF 2010 Estimation of the minimum detectable activity of preclinical PET imaging systems with an analytical method Medical Physics 37 6070–83 [PubMed: 21158319]

Blasberg R 2002 PET imaging of gene expression European Journal of Cancer 38 2137–46 [PubMed: 12387839]

Brunner SE and Schaart DR 2017 BGO as a hybrid scintillator / Cherenkov radiator for cost-effective time-of-flight PET Phys. Med. Biol 62 4421–39 [PubMed: 28358722]

Cherry SR, Sorenson JA and Phelps ME 2012 Physics in Nuclear Medicine E-Book (Elsevier Health Sciences)

van Dongen GAMS, Boellaard R and Vugts DJ 2020 In vivo tracking of single cells with PET Nature Biomedical Engineering 4 765–6

Du J, Ariño-Estrada G, Bai X and Cherry SR 2020 Performance comparison of dual-ended readout depth-encoding PET detectors based on BGO and LYSO crystals Phys. Med. Biol Online: http://iopscience.iop.org/article/10.1088/1361-6560/abc365

Du J, Bai X and Cherry SR 2018a A depth-of-interaction encoding PET detector module with dual-ended readout using large-area silicon photomultiplier arrays Phys. Med. Biol 63 245019 [PubMed: 30523925]

Du J, Bai X and Cherry SR 2019 Performance comparison of depth-encoding detectors based on dual-ended readout and different SiPMs for high-resolution PET applications Phys. Med. Biol 64 15NT03

Du J, Bai X, Gola A, Acerbi F, Ferri A, Piemonte C, Yang Y and Cherry SR 2018b Performance of a high-resolution depth-encoding PET detector module using linearly-graded SiPM arrays Phys. Med. Biol 63 035035 [PubMed: 29324437]

Du J, Wang Y, Zhang L, Zhou Z, Xu Z and Wang X 2009 Physical Properties of LYSO Scintillator for NN-PET Detectors 2009 2nd International Conference on Biomedical Engineering and Informatics 2009 2nd International Conference on Biomedical Engineering and Informatics pp 1–5

Du J, Yang Y, Bai X, Judenhofer MS, Berg E, Di K, Buckley S, Jackson C and Cherry SR 2016 Characterization of Large-Area SiPM Array for PET Applications IEEE Transactions on Nuclear Science 63 8–16 [PubMed: 27182077]

Freedenberg MI, Badawi RD, Tarantal AF and Cherry SR 2014 Performance and limitations of positron emission tomography (PET) scanners for imaging very low activity sources Physica Medica 30 104–10 [PubMed: 23680361]

Gambhir SS, Barrio JR, Phelps ME, Iyer M, Namavari M, Satyamurthy N, Wu L, Green LA, Bauer E, MacLaren DC, Nguyen K, Berk AJ, Cherry SR and Herschman HR 1999 Imaging adenoviral-directed reporter gene expression in living animals with positron emission tomography PNAS 96 2333–8 [PubMed: 10051642]

González AJ, Sánchez F, Majewski S, Parkhurst P, Vaigneur K and Benlloch JM 2016 Pilot Studies With BGO Scintillators Coupled to Low-Noise, Large-Area, SiPM Arrays IEEE Transactions on Nuclear Science 63 2482–6

Gu Z, Taschereau R, Vu NT, Wang H, Prout DL, Silverman RW, Bai B, Stout DB, Phelps ME and Chatziioannou AF 2013 NEMA NU-4 performance evaluation of PETbox4, a high sensitivity dedicated PET preclinical tomograph Phys. Med. Biol 58 3791–814 [PubMed: 23666034]

Gundacker S, Acerbi F, Auffray E, Ferri A, Gola A, Nemallapudi MV, Paternoster G, Piemonte C and Lecoq P 2016 State of the art timing in TOF-PET detectors with LuAG, GAGG and L(Y)SO scintillators of various sizes coupled to FBK-SiPMs J. Inst 11 P08008–P08008

Jung KO, Kim TJ, Yu JH, Rhee S, Zhao W, Ha B, Red-Horse K, Gambhir SS and Pratx G 2020 Whole-body tracking of single cells via positron emission tomography Nature Biomedical Engineering 4 835–44

Kang HG, Yamaya T, Han YB, Song SH, Ko GB, Lee JS and Hong SJ 2020 Crystal surface and reflector optimization for the SiPM-based dual-ended readout TOF-DOI PET detector Biomed. Phys. Eng. Express 6 065028

Kuang Z, Wang X, Fu X, Ren N, Yang Q, Zhao B, Zhang C, Wu S, Sang Z, Hu Z, Du J, Liang D, Liu X, Zheng H and Yang Y 2019 Dual-ended readout small animal PET detector by using 0.5 mm pixelated LYSO crystal arrays and SiPMs Nuclear Instruments and Methods in Physics Research Section A: Accelerators, Spectrometers, Detectors and Associated Equipment 917 1–8

Kuang Z, Wang X, Ren N, Wu S, Gao J, Zeng T, Gao D, Zhang C, Sang Z, Hu Z, Du J, Liang D, Liu X, Zheng H and Yang Y 2020 Design and performance of SIAT aPET: a uniform high-resolution small animal PET scanner using dual-ended readout detectors Phys. Med. Biol Online: http://iopscience.iop.org/10.1088/1361-6560/abbc83

Kwon SI, Gola A, Ferri A, Piemonte C and Cherry SR 2016 Bismuth germanate coupled to near ultraviolet silicon photomultipliers for time-of-flight PET Phys. Med. Biol 61 L38–47 [PubMed: 27589153]

Kyme AZ, Judenhofer MS, Gong K, Bec J, Selfridge A, Du J, Qi J, Cherry SR and Meikle SR 2017 Open-field mouse brain PET: design optimisation and detector characterisation Phys. Med. Biol 62 6207–25 [PubMed: 28475491]

LaBella A, Cao X, Petersen E, Lubinsky R, Biegon A, Zhao W and Goldan AH 2020 High Resolution Depth-Encoding PET Detector Module with Prismatoid Light Guide Array J Nucl Med jnumed.119.239343

Lewellen TK 2008 Recent developments in PET detector technology Phys. Med. Biol 53 R287–317 [PubMed: 18695301]

Li M, Wang Y and Abbaszadeh S 2020 Development and initial characterization of a high-resolution PET detector module with DOI Biomed. Phys. Eng. Express 6 065020 [PubMed: 34234961]

de Marcillac P, Coron N, Dambier G, Leblanc J and Moalic J-P 2003 Experimental detection of α-particles from the radioactive decay of natural bismuth Nature 422 876–8 [PubMed: 12712201]

Zhang Nan, Thompson CJ, Togane D, Cayouette F and Nguyen KQ 2002 Anode position and last dynode timing circuits for dual-layer BGO scintillator with PS-PMT based modular PET detectors IEEE Transactions on Nuclear Science 49 2203–7

Ouyang Y, Kim TJ and Pratx G 2016 Evaluation of a BGO-Based PET System for Single-Cell Tracking Performance by Simulation and Phantom Studies Mol Imaging 15 1536012116646489

Pizzichemi M, Polesel A, Stringhini G, Gundacker S, Lecoq P, Tavernier S, Paganoni M and Auffray E 2019 On light sharing TOF-PET modules with depth of interaction and 157 ps FWHM coincidence time resolution Phys. Med. Biol 64 155008 [PubMed: 31239430]

Popov V, Majewski S and Weisenberger AG 2003 Readout electronics for multianode photomultiplier tubes with pad matrix anode layout 2003 IEEE Nuclear Science Symposium. Conference Record (IEEE Cat. No.03CH37515) 2003 IEEE Nuclear Science Symposium. Conference Record (IEEE Cat. No.03CH37515) vol 3 pp 2156–2159 Vol.3

Ren S, Yang Y and Cherry SR 2014 Effects of reflector and crystal surface on the performance of a depth-encoding PET detector with dual-ended readout Medical Physics 41 072503 [PubMed: 24989406]

Shao Y, Sun X, Lan KA, Bircher C, Lou K and Deng Z 2014 Development of a prototype PET scanner with depth-of-interaction measurement using solid-state photomultiplier arrays and parallel readout electronics Phys. Med. Biol 59 1223–38 [PubMed: 24556629]

Shao Y, Yao R and Ma T 2008 A novel method to calibrate DOI function of a PET detector with a dual-ended-scintillator readout Medical Physics 35 5829–40 [PubMed: 19175139]

Sharma V, Luker GD and Piwnica-Worms D 2002 Molecular imaging of gene expression and protein function in vivo with PET and SPECT Journal of Magnetic Resonance Imaging 16 336–51 [PubMed: 12353250]

Wong W, Li H, Zhang Y, Ramirez R, An S, Wang C, Liu S, Dong Y and Baghaei H 2015 A High-Resolution Time-of-Flight Clinical PET Detection System Using a Gapless PMT-Quadrant-Sharing Method IEEE Transactions on Nuclear Science 62 2067–74

Yang Q, Kuang Z, Sang Z, Yang Y and Du J 2019 Performance comparison of two signal multiplexing readouts for SiPM-based pet detector Phys. Med. Biol 64 23NT02

Yoshida E, Obata F, Kamada K and Yamaya T 2020 A crosshair light sharing PET detector with DOI and TOF capabilities using four-to-one coupling and single-ended readout IEEE Transactions on Radiation and Plasma Medical Sciences 1–1

Zhang H, Vu NT, Bao Q, Silverman RW, Berry-Pusey BN, Douraghy A, Williams DA, Rannou FR, Stout DB and Chatziioannou AF 2010 Performance Characteristics of BGO Detectors for a Low Cost Preclinical PET Scanner IEEE Transactions on Nuclear Science 57 1038–44 [PubMed: 21165154]

Figure 1.

Photographs of the (left) wo-ILG BGO array, (middle) wp-ILG BGO array, and (right) wf-ILG BGO array.

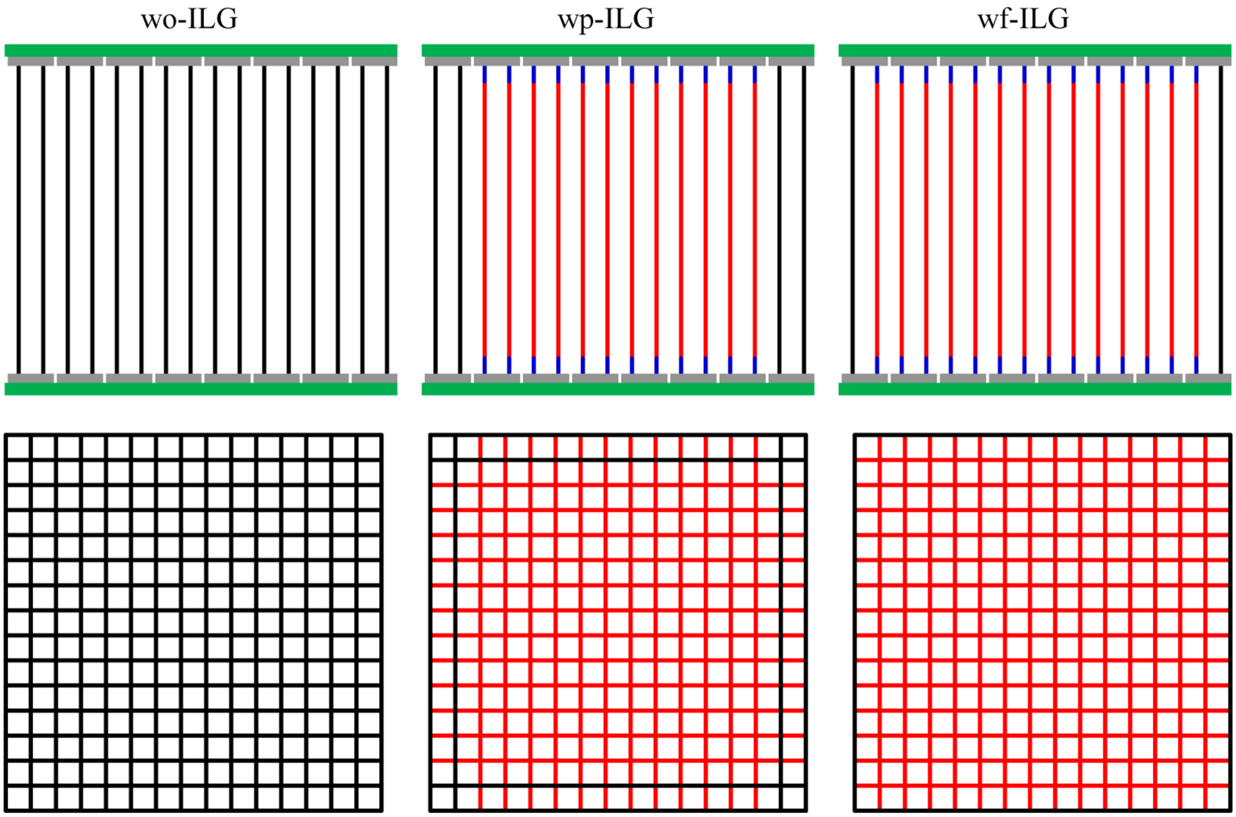

Figure 2.

Schemas of the BGO arrays. (Top row) side views and (bottom row) transverse views of the BGO arrays. The black lines indicate the reflectors with a length of 20 mm, the red lines indicate the reflectors with a length of 18 mm, and the blue lines (1 mm long) indicate the transparent gaps between BGO elements that were filled with optical glue OP-30. The gray and blue rectangles in these top figures indicate the printed circuit boards (PCBs) and the SiPM pixels, respectively.

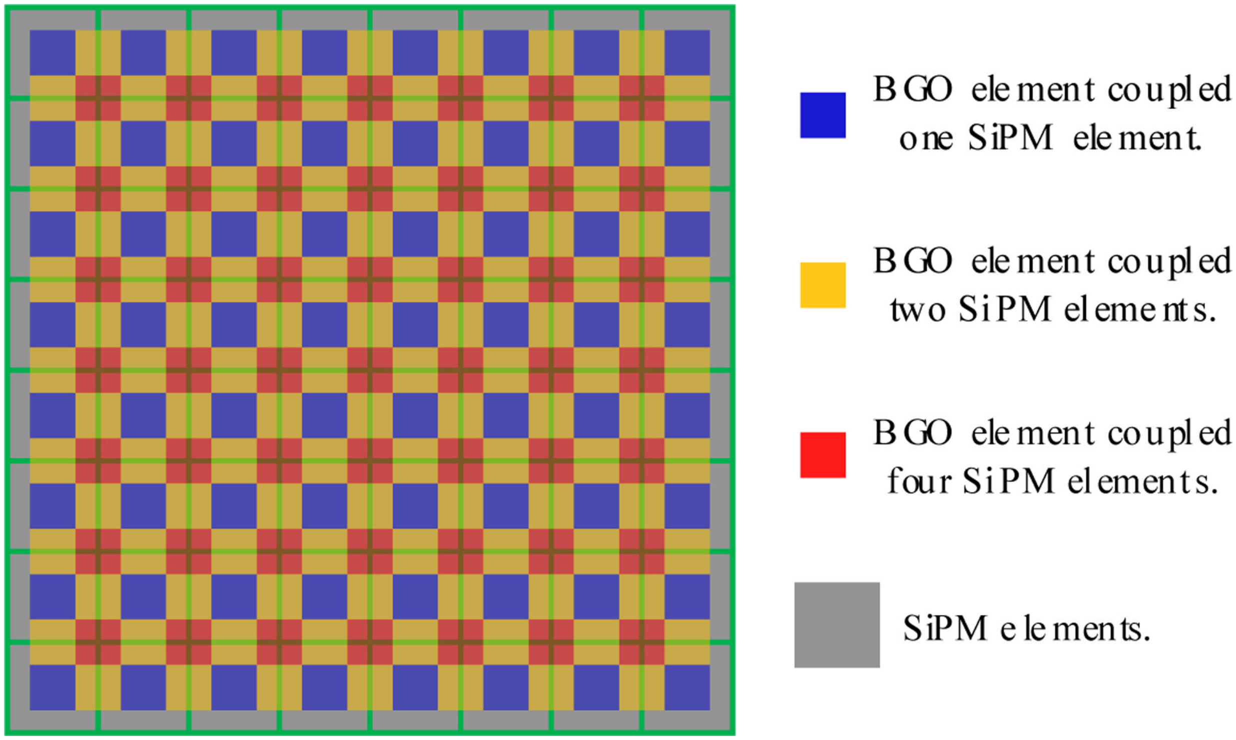

Figure 3.
Schema of the concentric SiPM array and BGO array. The green lines indicate the edges of the SiPMs. The blue, yellow, and red squares indicate the areas of the BGO elements.

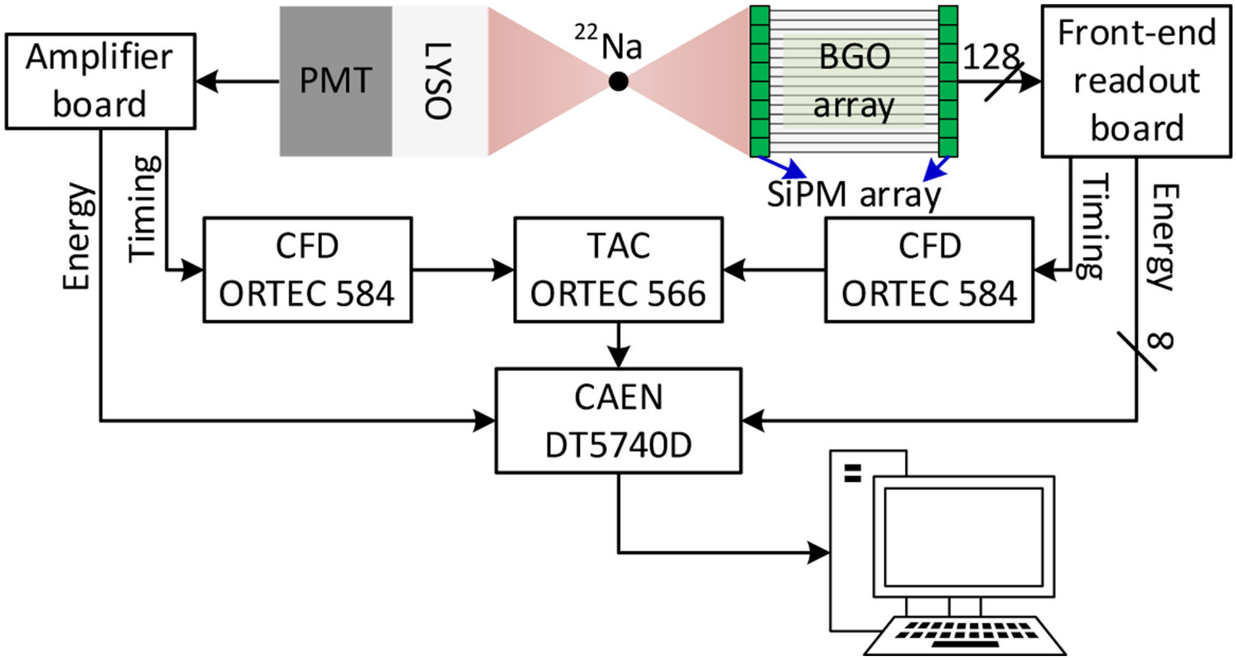

Figure 4.

Simplified schema of the experimental setup with readout electronics for flood histogram and timing resolution measurements. During the DOI resolution measurement, the dual-ended readout detector was irradiated from one side (Yang *et al* 2019).

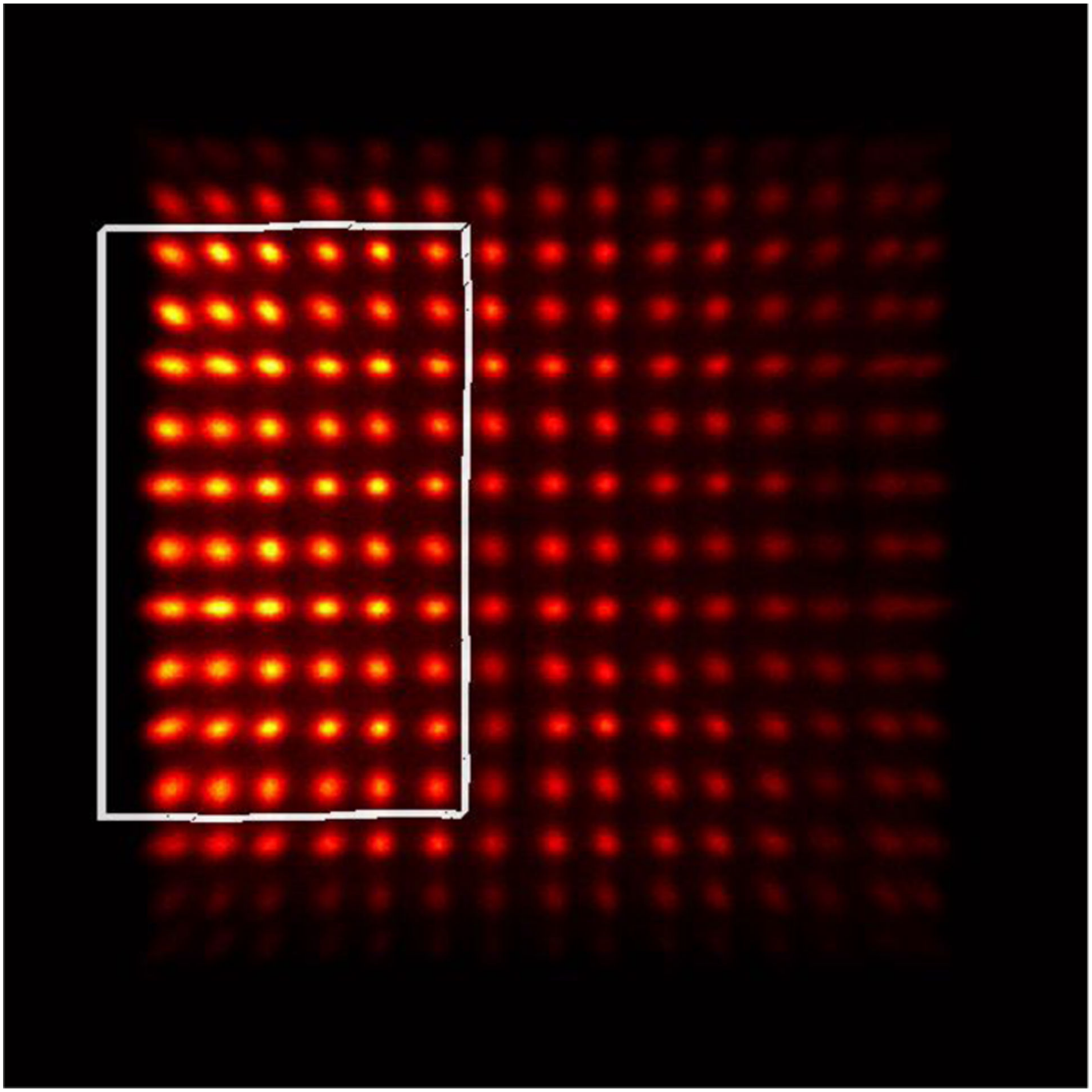

Figure 5.
Flood histogram obtained during DOI resolution measurements. The 6 × 10 crystals in the white rectangle were used as representative crystals to measure the DOI resolution of the detector.

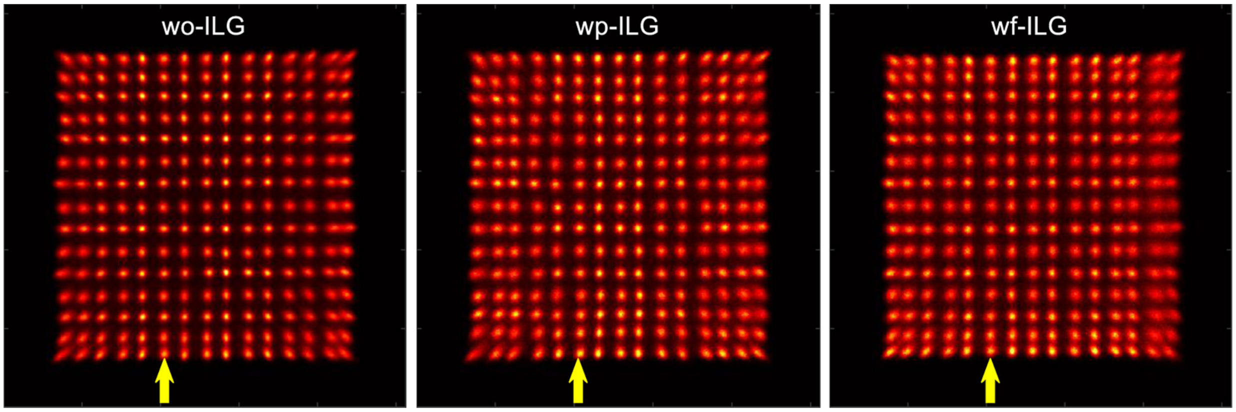

Figure 6.

Flood histograms of the (left) wo-ILG detector, (middle) wp-ILG detector, and (right) wf-ILG detector.

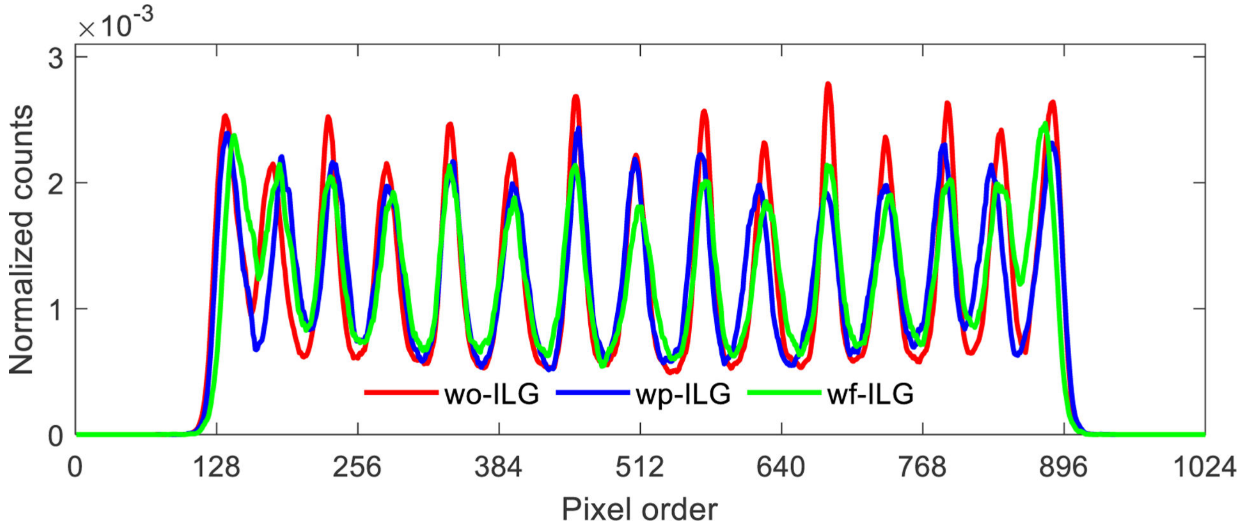

Figure 7.

Position profiles of the 6th crystal column shown in figure 6, which are indicated by yellow arrows.

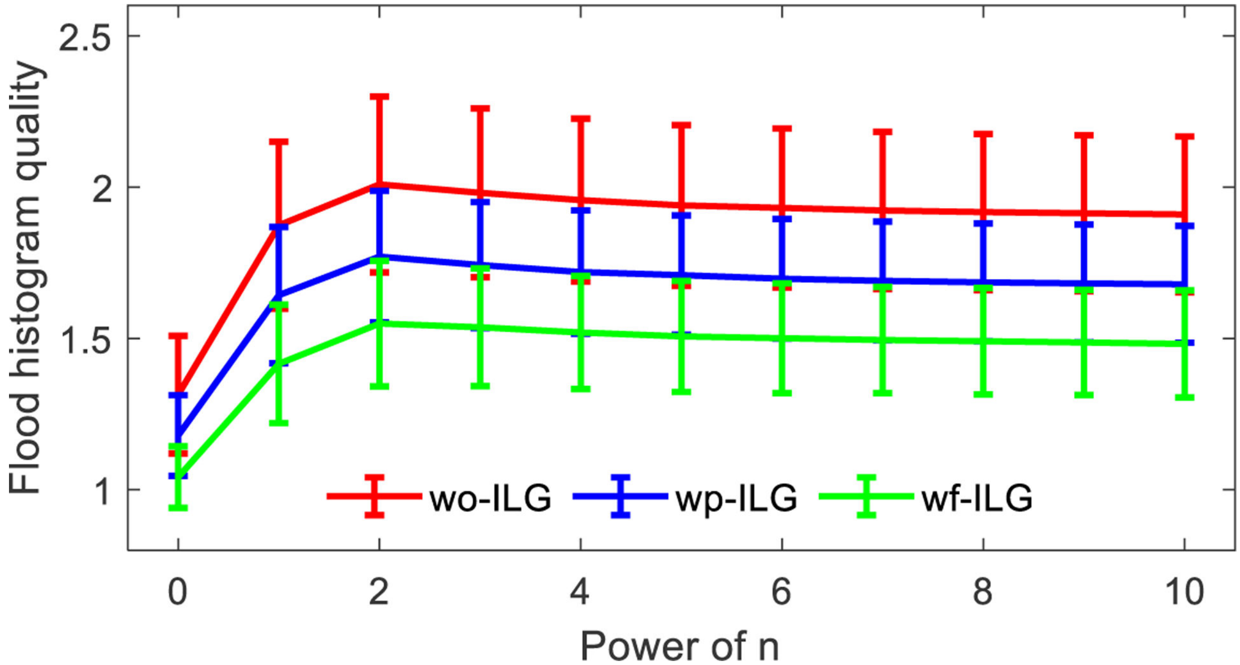

Figure 8.

Flood histogram qualities obtained using different weighting factors. The error bars are the standard deviation values of the flood histogram quality values across all crystals. *n* is the weighting factors of energy shown in equation (1).

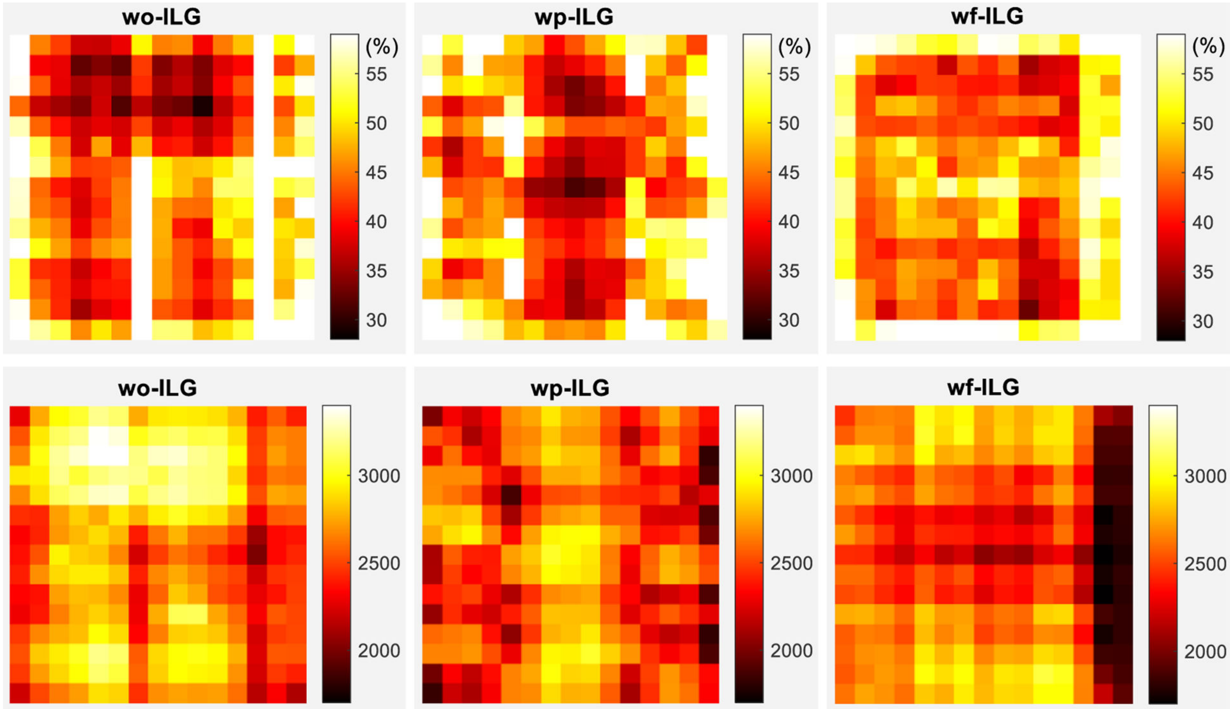

Figure 9.
(top row) energy resolution and (bottom row) 511 keV photopeak position for each crystal of the (left) wo-ILG detector, (middle) wp-ILG detector, and (right) wf-ILG detector.

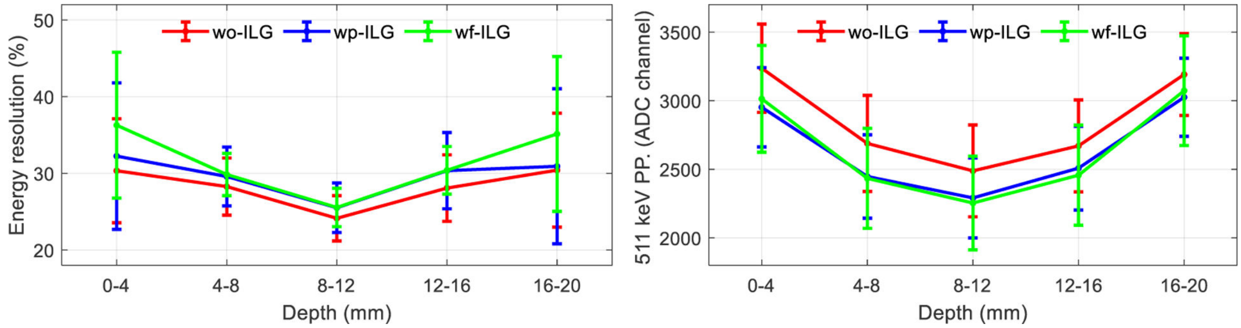

Figure 10.

(left) energy resolution and (right) photopeak position versus depth. Depth 0 mm was closed to the radiation source. The error bars are the standard deviation values of the energy resolution or 511 keV photopeak position across all crystals.

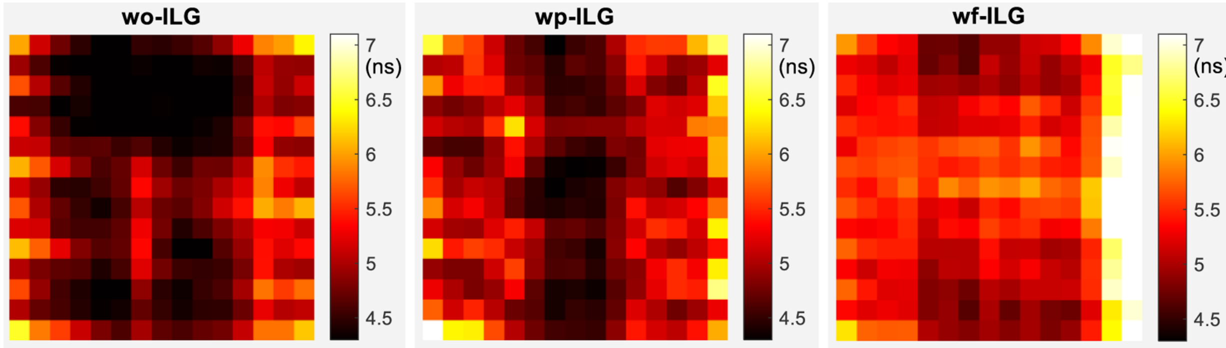

Figure 11.

Timing resolutions for each crystal of the (left) wo-ILG detector, (middle) wp-ILG detector, and (right) wf-ILG detector.

and (right) wf-ILG detector.

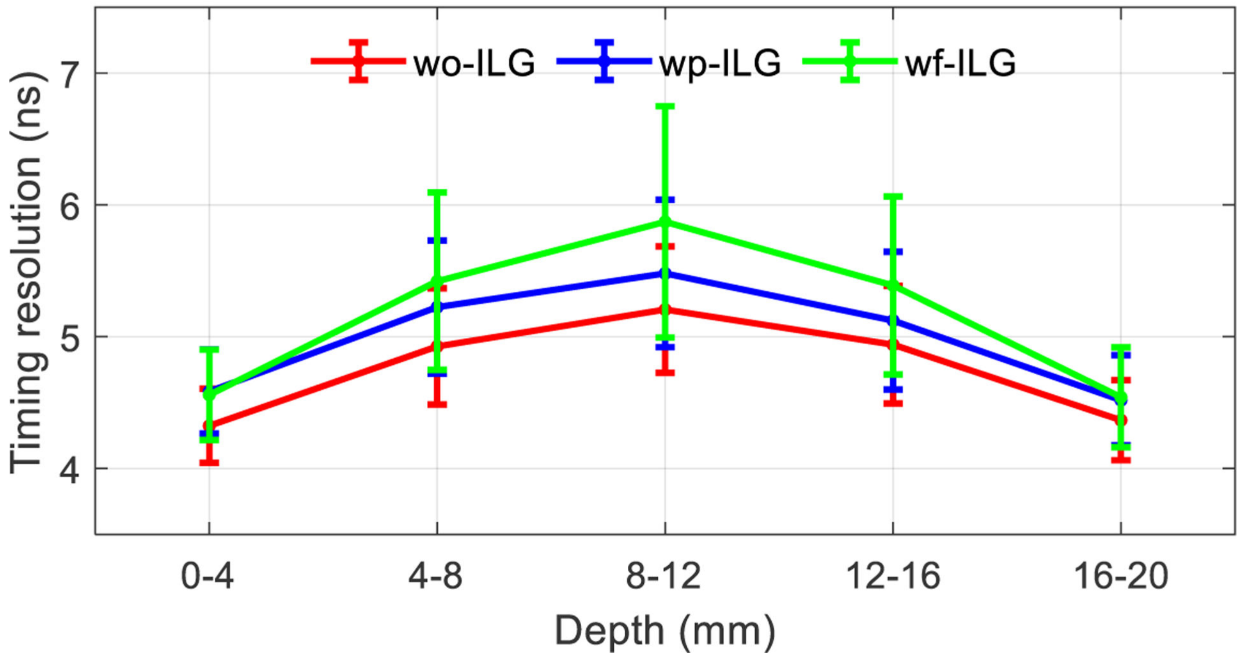

Figure 12.

Average timing resolutions across all crystals versus the depth for the three detectors investigated. The error bars are the standard deviation values of the timing resolution across all crystals.

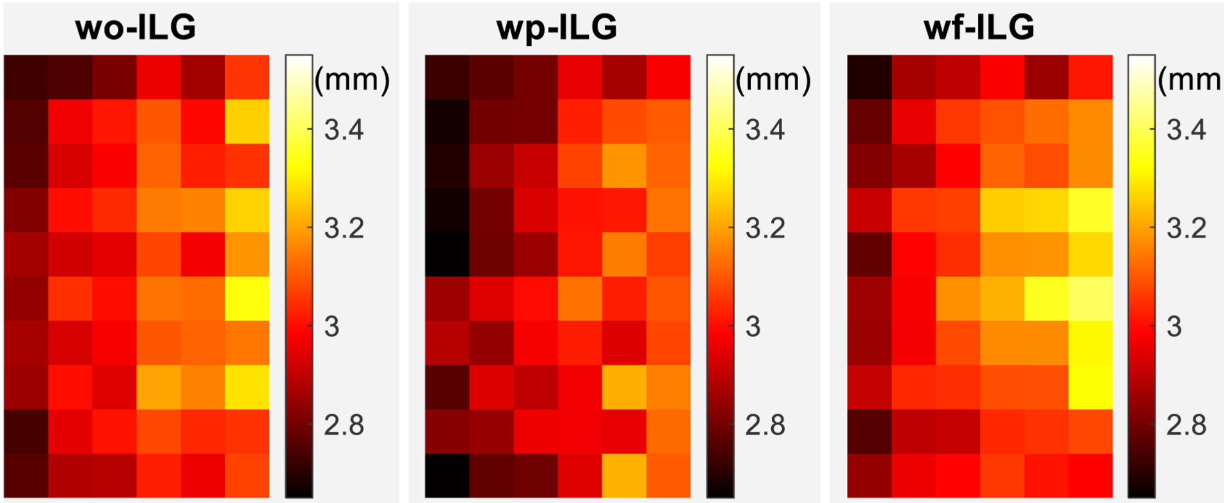

Figure 13.

DOI resolution for each crystal of the (left) wo-ILG detector, (middle) wp-ILG detector, and (right) wf-ILG detector.

Author Manuscript

Author Manuscript

Author Manuscript

Table I.

Summary of the performance of the three detectors.

		wo-ILG detector	wp-ILG detector	wf-ILG detector
Flood histogram quality		2.1 ± 0.3	1.8 ± 0.2	1.6 ± 0.2
Energy resolution (%)	w/ DOI correction	44.3 ± 6.6	44.9 ± 6.4	43.9 ± 6.4
	w/o DOI correction	27.2 ± 3.9	28.7 ± 4.6	29.5 ± 4.7
Timing resolution (ns)	w/ DOI correction	4.7 ± 0.5	4.9 ± 0.5	5.0 ± 0.6
	w/o DOI correction	4.8 ± 0.4	5.0 ± 0.4	5.1 ± 0.5
DOI resolution (mm)		3.0 ± 0.2	2.9 ± 0.2	3.0 ± 0.2